

UNCLASSIFIED

Defense Technical Information Center  
Compilation Part Notice

ADP013624

TITLE: Industrial Applications of LES in Mechanical Engineering

DISTRIBUTION: Approved for public release, distribution unlimited

This paper is part of the following report:

TITLE: DNS/LES Progress and Challenges. Proceedings of the Third  
AFOSR International Conference on DNS/LES

To order the complete compilation report, use: ADA412801

The component part is provided here to allow users access to individually authored sections of proceedings, annals, symposia, etc. However, the component should be considered within the context of the overall compilation report and not as a stand-alone technical report.

The following component part numbers comprise the compilation report:

ADP013620 thru ADP013707

UNCLASSIFIED

# INDUSTRIAL APPLICATIONS OF LES IN MECHANICAL ENGINEERING

CHISACHI KATO

*Institute of Industrial Science*

*University of Tokyo, Tokyo, Japan*

MASAYUKI KAIHO, AKIRA MANABE

*Mechanical Engineering Research*

*Laboratory*

*Hitachi LTD., Ibaraki, Japan*

## Abstract

This paper describes industrial applications of LES with a particular emphasis on internal-flow simulations of turbomachinery and simulations of aeroacoustics. The aerodynamic sound is assumed to be generated by flows, at relatively low Mach numbers, around an object, and it is therefore calculated from fluctuating surface-pressure as obtained by the LES. In order to deal with a moving boundary interface in the flow field, a form of the finite-element method in which overset grids are applied from multiple dynamic frames of reference has been developed. The overset-grid approach is also applied to increase the grid resolution around the body of interest for computations in the field of aeroacoustics. The method is implemented as a parallel program by applying a domain-decomposition programming model. The validity of the proposed method is shown through two numerical examples: prediction of the internal flows of a hydraulic pump stage and prediction of the far-field sound that results from unsteady flow around an insulator mounted on a high-speed train.

## 1. Introduction

At present, the Reynolds-averaged Navier-Stokes (RANS) equations are used as the governing equations in most computations of flow field for engineering applications. Since the RANS equations are in terms of time averages, computation with RANS has inherent limitations in predicting the unsteady nature of a flow field. Solutions from the RANS equations usually deteriorate when the flow field of interest involves the large-scale separations that are often encountered in engineering applications. On the other hand, the large eddy simulation (LES), in which turbulent eddies of a scale larger than the

computational grid are directly computed, has the potential to predict unsteady flows and/or flow fields that include regions of large-scale separation much more accurately than RANS-based computation does in general. The goal of the present study is to develop a practical engineering tool that is based on LES, with a particular emphasis on internal-flow simulations of turbomachinery and simulations of aeroacoustics.

## 2. Governing Equations

### 2.1 Flow-Field Computation

The governing equations on which the present study is based are the spatially filtered continuity equation and Navier-Stokes equations for the flow of an incompressible fluid, as represented in Cartesian coordinates. The inertial forces associated with the motion of the frames of reference are added to Navier-Stokes equations. The standard Smagorinsky model<sup>1</sup>, incorporated with the Van-Driest wall-damping function that represents the near-wall effects, is adopted as the subgrid-scale model of turbulence. The Smagorinsky coefficient is fixed to 0.15, which is a standard value for flows with large separation, and the grid-filter size is computed as the cube-root of the volume of each finite element.

### 2.2 Computation of the Acoustic Field

In the present study, the aerodynamic sound is assumed to be generated by flows, at relatively low Mach numbers, around an object whose dimension is much smaller than the wavelength of sound. In this case, the far-field sound radiated from the unsteady flow can be calculated from Curle's equation<sup>2</sup>:

$$p_a = \frac{1}{4\pi a} \frac{x_i}{r^2} \frac{\partial}{\partial t} \int_S n_i p(y, t - r/a) dS \quad (1)$$

where  $a$  denotes the speed of sound in the ambient fluid,  $p$  the static pressure in the flow field,  $p_a$  the far-field sound pressure,  $x_i$  the location of the sound-observation point,  $y$  the coordinates at the noise source,  $r$  the distance between the noise source and the sound-observation point, and  $n_j$  the outward unit vector normal to the solid boundaries. In the above expression, the assumption that the flow has a high Reynolds number makes the contribution of viscous stresses to the surface integral negligible. It is thus possible to calculate the far-field sound from the fluctuating surface pressure as obtained by the LES.

## 3. Numerical Method

### 3.1 Overset Grids from Multiple Dynamic Frames of Reference

In the present study, a moving boundary interface in the flow field is treated with overset grids from multiple dynamic frames of reference<sup>3</sup>. The application of this method to the interaction between a rotating impeller and a stationary casing in a pump is schematically depicted in **figure 1**. A computational mesh that rotates along with the impeller is used to compute the flow within the impeller. On the other hand, a dedicated stationary computational mesh for each part computes the flow in stationary parts of the pump. Each mesh includes appropriate margins of overlap with its neighboring meshes upstream and downstream. At every time step, the velocity components and static pressure within each such margin are the values interpolated in the computational mesh of the corresponding neighbor. Element-wise tri-linear functions are used to interpolate both the velocity components and the static pressure<sup>4,5</sup>. When velocity components are overset, an appropriate coordinate transformation must be applied to take the differences between the frames of reference into account.

### 3.2 Finite-Element Formulation

A streamline-upwind finite-element formulation<sup>6</sup> is used to discretize the governing equations of the flow field. This formulation is based on the explicit Euler's method, but shifts the spatial residuals of the governing equations in the upstream direction of the local flow. The magnitude of this shift is one half of the time increment multiplied by the magnitude of the local flow velocity. This shift exactly cancels out the negative numerical dissipation that is otherwise the result of applying Euler's method and guarantees stability and the accuracy of solutions. The proposed formulation essentially possesses second-order accuracy in terms of both time and space, and has been successfully applied to the LES of external as well as internal flows<sup>3,6,7</sup>.

### 3.3 Parallel Implementation

We have implemented the formulation described in the previous sections as a parallel program by using the domain-decomposition programming model. In this programming model, the global computational domain is partitioned into a prescribed number of subdomains (see **figure 2** for an example of mesh partitioning), and each of the subdomains is assigned to a dedicated processing node. The communicating pairs and/or local coordinates where given interpolations are taking place change at the moving-boundary interfaces on every time step. The usual (unsophisticated) parallel implementation therefore includes broadcast communications on every time step as the processing node searches for its new communication pairs. This communication overhead seriously deteriorates the overall parallel computing performance. In the present

study, the communication pairs are searched in advance by a serial computation and they are fed to the parallel flow solver as input data on every time step. This procedure not only avoids the otherwise inevitable communications overhead but also brings in greater flexibility with the flow solver. By preparing appropriate input data for the moving-boundary interfaces, the flow solver is capable of computing flow fields with an arbitrary number of moving-boundary interfaces that move in an arbitrary (but defined) manner. The performance of the proposed method in terms of parallel computing was evaluated on various hardware platforms. **Table 1** shows one such example, where the method was tested on Hitachi's SR8000 super-computer. The sustained performance ranges from 12% to 14% of the peak performance. **Figure 3** is a plot of the overall sustained performance against the number of the processing nodes for the same benchmark test. A parallel computing efficiency of over 85% is achieved on this platform and this confirms that it is possible to complete a large-scale computation of flow with a grid that has more than 10 million divisions within a practical period of time on a high-end computer of the current generation.

#### 4. Simulation Examples

After ensuring the validity of the LES code we developed by applying it to the calculation of basic flows of various types<sup>6,7</sup>, the code is now being tested on real-world problems. Two examples will be described below: one from the simulation of turbomachinery and the other from aeroacoustical simulations.

##### 4.1 Simulation of Unsteady Flow in a Mixed-Flow Pump

The code was applied to the computation of the internal flow in a mixed-flow pump stage with a high designed specific-speed. The measured total heads of this pump exhibited slightly unstable characteristics at a flow-rate ratio of around 60%. In order to obtain comparative data for use in validation, the mean-velocity profiles at the impeller's inlet and exit cross-sections were measured by a two-dimensional LDV.

The computational mesh used in this study is shown in **figure 4**. At the upstream of the regulation-plate mesh, a driving section (not shown in this figure) is overset, and therefore, on every time step, the inlet velocities of the regulation-plate mesh were the values interpolated from instantaneous velocities of the driving section (see **figures 5** and **6**, respectively for typical instantaneous secondary-flow velocity and fluctuations in centerline velocities in this section). The flow rate of the pump was set by adjusting the magnitude of uniform acceleration that was applied to the driving section in the axial direction (see **figure 7** for a comparison of the measured and predicted mean-velocity profiles in the driving section). The Reynolds number based on the impeller's exit

diameter  $D_2$  and the circumferential velocity  $u_2$  at this point is  $5.7 \times 10^6$ . In order to investigate effects of grid resolution on the accuracy of the solution, two sets of meshes with different grid resolution were used. The numbers of elements are approximately 1.7 million for the coarse mesh and 5 million for the fine mesh. The time increment was set so that 8,000 time steps corresponded to a single revolution of the impeller and the total pump head and mean-velocity distributions were evaluated by averaging the flow field during 10 impeller's revolutions. The computations were carried out by using 16 processing nodes on the Hitachi SR8000 super-computer. The required CPU time was about 1.6 seconds per time step for the fine-mesh LES. The total CPU time for a single flow-rate ratio was thus about 35 hours for this case.

The computed total pump-heads, together with their measured equivalents, are plotted in **figure 8**. The total pump-heads predicted by the fine-mesh LES agree fairly well with the measured values down to a flow-rate ratio of 60%, where the measured head-flow characteristics indicate an onset of the total stall. The fine-mesh LES predicted an onset of the total stall at a flow-rate ratio of 54%, which is 6% lower than the measured value. In the following, we are presenting flow fields at flow-rate ratios of 60% and 43% as they respectively represent the pre-stall and post-stall flow fields. **Figure 9** shows instantaneous distributions of axial velocity in the centerline plane of the pump. **Figure 10** shows the computed and measured mean-velocity profiles at the impeller's inlet cross-section (see figure 9 for its location) where  $C_m$  and  $C_u$  respectively denote the meridional and circumferential velocities. The fine mesh LES accurately predicts, for the post-stall case, the large region of reverse flow near the impeller's tip and intense pre-rotation that results from this reverse flow and results in the decrease in the total pump head. Finally, **figure 11** shows mean-velocity profiles at the impeller's exit section. The velocity profiles predicted by the fine-mesh LES are in reasonably good agreement with the measured profiles and the changes in the flow pattern to the centrifugal type at the post-stall condition are clearly captured by the fine-mesh LES. The hydrodynamic mechanism in which characteristics instability occurs is now being investigated by using the simulated flow-field data, which will hopefully lead us to the establishment of a general design rule for avoiding this occurrence.

#### 4. 2 Aeroacoustical Simulation of a Pantograph Insulator

To achieve further increases in the speeds of high-speed trains, which is presently running at 300 km/h in Japan, a reduction in the generation of aerodynamic noise by the pantograph (the electric-current collector on the train's roof) has become a matter of great concerns in terms of the aerodynamic design of the vehicle. Past research has indicated that, among the various noise sources of a pantograph, the insulator provides the dominant contribution to the overall level of noise. We have therefore simulated the near-wake of flow around an

insulator and the resulting far-field sound, with the particular aim of identifying the primary source of noise<sup>8</sup>.

**Figures 12 and 13** show an overset mesh for the near-wake LES of the insulator that was simulated in the present study. Two sets of overset grids with different resolution were used in the LES and the effects of grid resolution on the fluctuations in the near wake as well as on the resulting far-field sound were investigated. The numbers of elements are approximately 2 million for the coarse mesh and 6 million for the fine mesh. In the following, we are presenting results from the fine-mesh LES unless we state otherwise.

To illustrate the temporal wake structure, regions of instantaneous reverse flow are shown in **figure 14**. The boundary layer that develops on the surface of the insulator separates from the surface while the flow is still laminar, but a transition to turbulence takes place soon after that. **Figure 15** shows an instantaneous distribution of streamwise velocity in the insulator's mid-height plane. The wake still possesses a large vortical structure, similar to the well-known Karman vortex, but this large structure is rather weak due to the enhancement of spanwise mixing effects by the circular disks. **Figure 16** shows the instantaneous distribution of static-pressure on the insulator's surface and base plate.

Typical fluctuations in streamwise velocity in the near wake and their power spectra, for both the coarse- and fine-mesh cases, are shown in **figure 17**. The frequency range that is resolvable by the coarse-mesh LES has its upper bound at a Strouhal number of approximately 1.0 (five times the usual Karman vortex frequency). The upper bound is extended to a Strouhal number of about 6 by the fine-mesh LES.

The fluctuations in far-field sound pressure and the power spectra of these fluctuations are shown in **figure 18**, for both the coarse-mesh and fine-mesh cases, together with the experimental value as measured in a wind tunnel. For convenience, the sound pressure are converted to actual values that correspond to a vehicle speed of 350 km/h (97.2 m/s) by assuming the Reynolds number similarity of the flow fields for the model and for the actual structure. The sound-pressure levels predicted by the coarse-mesh LES and the fine-mesh LES are surprisingly different. The fine-mesh LES provides a reasonably good prediction of the sound-pressure level at frequencies up to around 2.5 kHz, which corresponds to the Strouhal number of 6.4. This is approximately identical to the resolved frequency range for the near-wake velocity fluctuations.

Finally, the instantaneous sound-source distributions are investigated according to Powell's equation<sup>9</sup>. **Figure 19** shows the instantaneous distributions of the sound source term, which are obtained from the LES. By examining these sound-source distributions, the longitudinal vortices generated by the circular

disks are identified as being primarily responsible for the generation of sound by this flow.

The two examples mentioned above (and many others not given here) have clearly indicated that LES is now beginning to serve as a vital design tool in at least some cases of mechanical engineering.

## 5. Conclusions

Large eddy simulation has been applied to the prediction of internal flows in turbomachinery and aerodynamic sound that results from unsteady flow around a complex object. The standard Smagorinsky model, incorporated with the Van-Driest damping function, is adopted as the subgrid-scale model. The numerical method is based on a streamline-upwind finite-element formulation with accuracy of the second-order in both time and space, and incorporates the application of overset grids from multiple and dynamic frames of reference. The method is implemented as a parallel program by a domain-decomposition programming model.

Initially, the internal flow of a high-specific-speed mixed-flow pump stage was simulated, as a way of evaluating the validity of the proposed method. The predicted total pump-head and mean-velocity distributions at the impeller's inlet and exit cross-sections were in good agreement with the measured values. The near wake and the resulting far-field sound were then computed for flow around an insulator mounted on a high-speed train. The predicted sound-pressure level was also in reasonably good agreement with the wind-tunnel measurement.

The proposed method thus seems to be a promising candidate for use as an aerodynamic/aeroacoustic design tool in the next decade.

## References

1. Smagorinsky, J., 1963, *Mon. Weath. Rev.*, **Vol. 91**, No. 3, pp. 99-164.
2. Curle, N., 1955, *Proc. Roy. Soc.*, **A231**.
3. Kato, C., et al., 1999, *ASME-FEDSM99-7802*.
4. Ikegawa, M., et al., 1994, *Comput. Methods Appl. Mech. Engrg.*, **Vol. 112**, pp. 149-163.
5. Kaiho, M., et al., 1997, *Int. J. Numer. Meth. Fluids*, **Vol. 24**, pp. 1341-1352.
6. Kato, C., and Ikegawa, M., 1991, *ASME FED-Vol. 117*, pp. 49-56.
7. Kato, C., et al., 1993, *AIAA Paper 93-0145*.
8. Kato, C., et al., 2000, *AIAA Paper 2000-1942*.
9. Powell, A., 1964, *J. of Acoust. Soc. Am.*, **Vol. 33**, pp. 177-195.

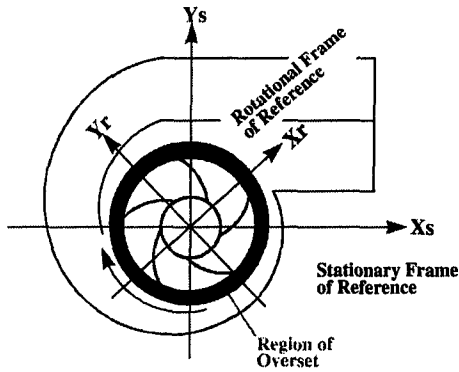


Figure 1. Schematic view of an example of overset grids from dual frames of reference.

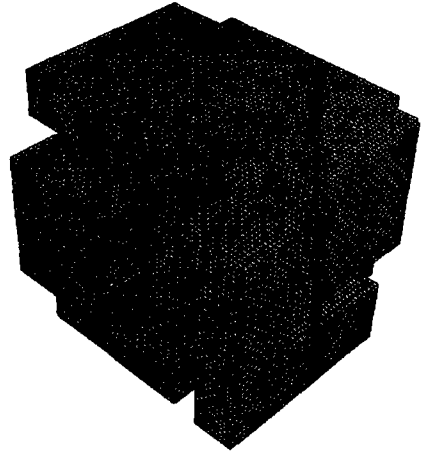


Figure 2. Example of a sub-domain mesh partitioned by the recursive graph-bisection method (computational mesh for flow in a cubic cavity partitioned into 8 sub-domains).

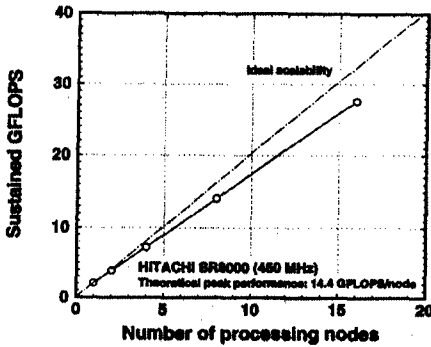


Figure 3. Sustained parallel computing performance

Table 1. Results of benchmark tests (CPU time needed to advance by a single time step in a cubic-cavity flow simulation on Hitachi's SR8000).

Number of processing nodes	1	2	4	8	16
Number of elements in millions	1.0	2.0	4.0	8.0	16.0
Seconds taken by CPU per time step	3.45	3.62	3.89	3.99	4.06
Sustained GFLOPS	2.03	3.87	7.23	14.04	27.60
Ratio of sustained to peak performance (%)	14.1	13.4	12.6	12.2	12.0

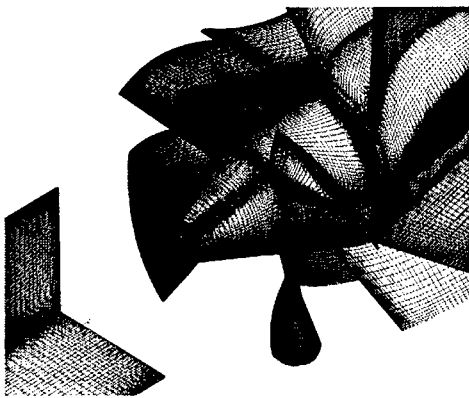
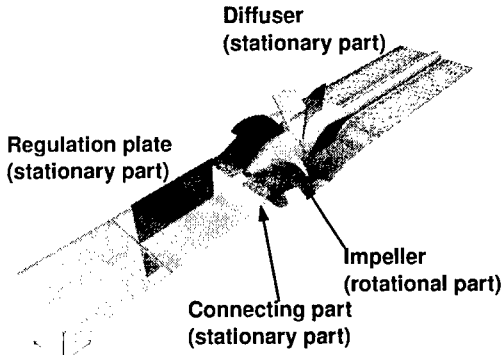


Figure 4. Computational mesh for a mixed-flow pump stage, composed of meshes for 5 parts (note: the mesh for the inlet driving-section is not shown here).

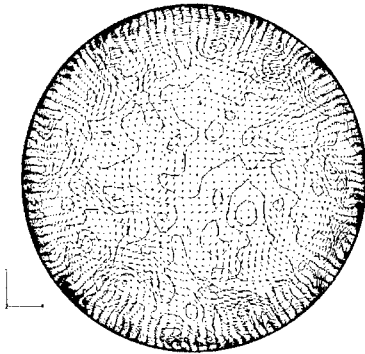


Figure 5. Instantaneous distribution of secondary flow in the driving section.

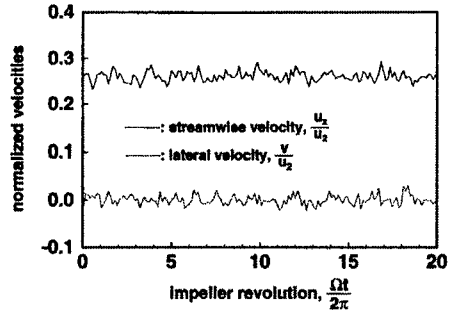


Figure 6. Fluctuations in centerline velocities in the driving section.

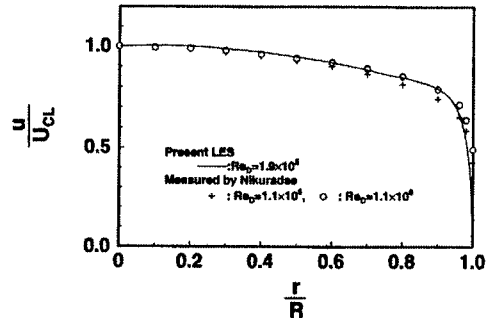


Figure 7. Time-averaged distribution of streamwise velocity in the driving section.

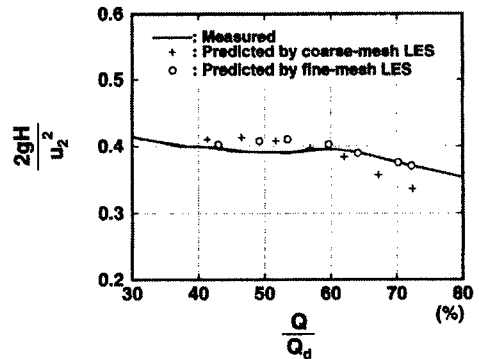


Figure 8. Comparison of measured and predicted head-flow characteristics.

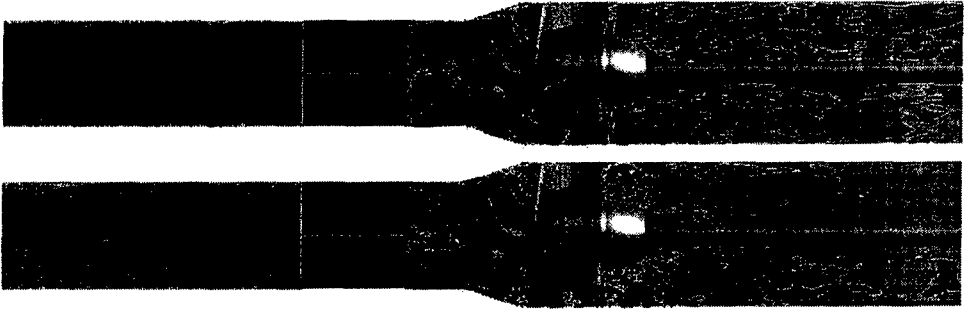


Figure 9. Instantaneous distributions of axial velocity component for  $Q=60\%$  (upper) and  $Q=43\%$  (lower) [fine-mesh LES]. Black lines in the upper figure indicate the approximate locations where velocity profiles were measured by a two-dimensional LDV for the impeller's inlet and exit cross-section.

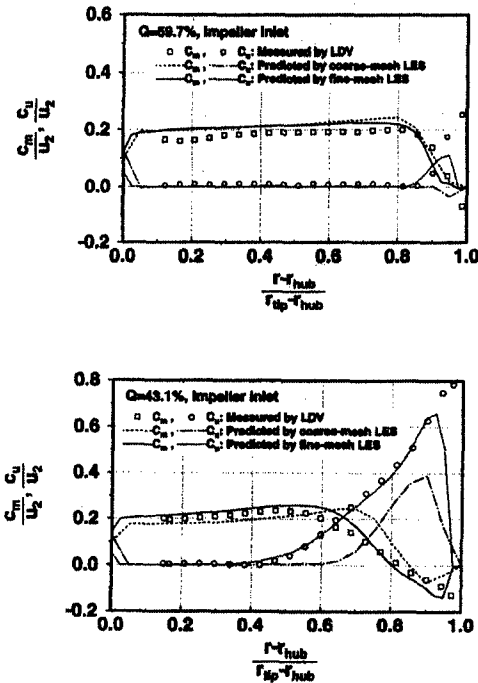


Figure 10. Predicted and measured distributions of phase-averaged velocities at the impeller's inlet cross-section for  $Q=60\%$  (upper) and  $43\%$  (lower).

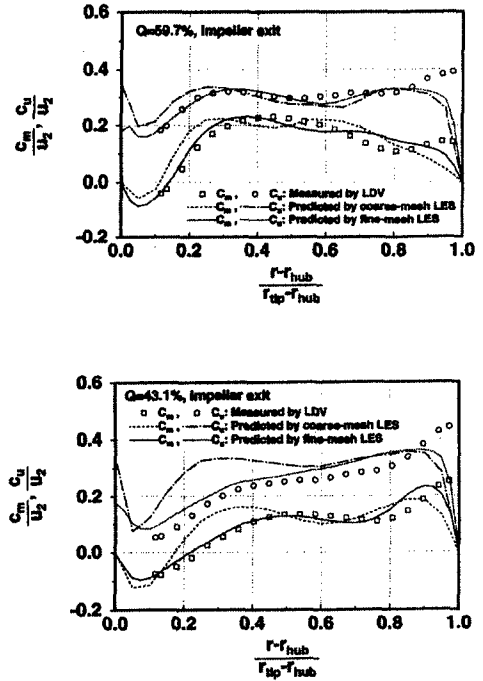
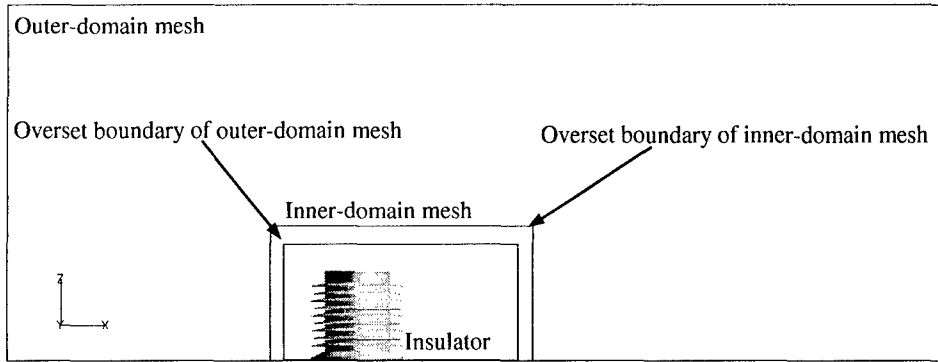
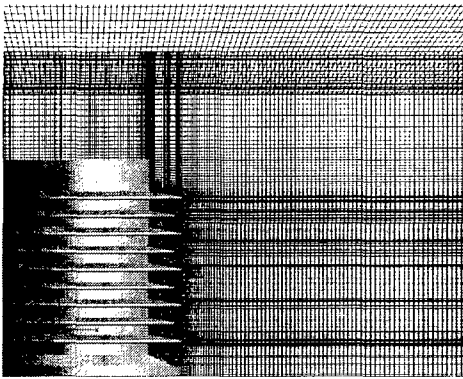


Figure 11. Predicted and measured distributions of phase-averaged velocities at the impeller's exit cross-section for  $Q=60\%$  (upper) and  $43\%$  (lower).



**Figure 12.** Computational region for an overset LES of unsteady flow around an insulator



**Figure 13.** Overset meshes for flow around an insulator (fine-mesh case).

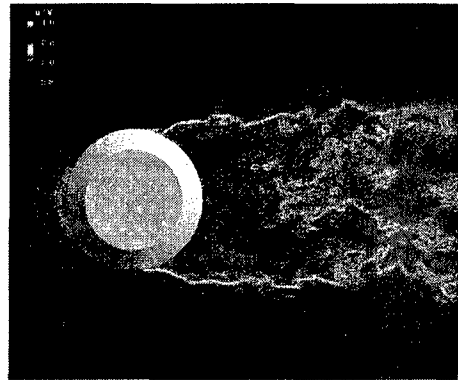


**Figure 15.** Instantaneous distribution of streamwise-velocity

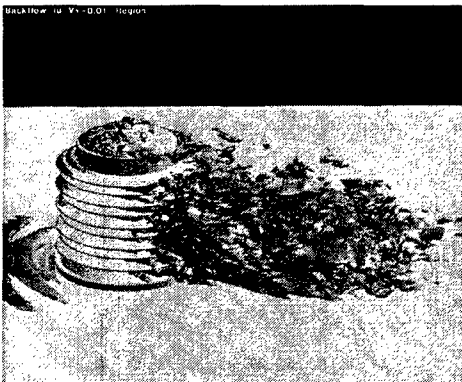


**Figure 14.** Regions of instantaneous reverse flow.

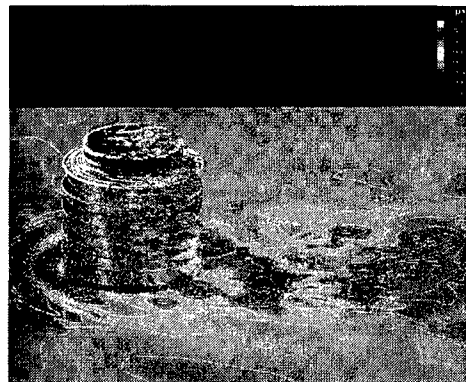


**Figure 16.** Instantaneous distribution of surface pressure.

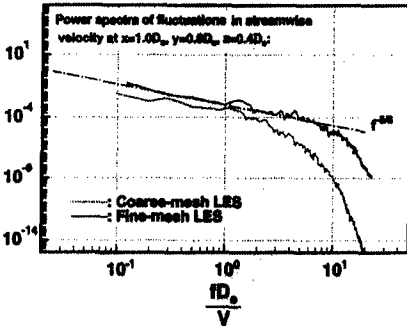
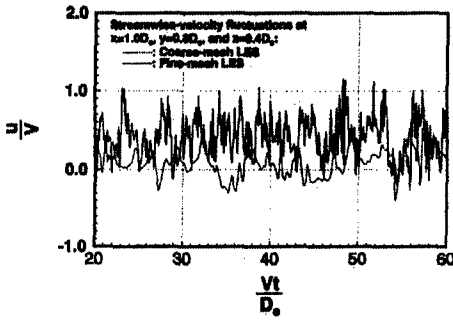


Figure 17. Fluctuations in streamwise velocity in the near wake (upper) and the power spectra of these fluctuations (lower).

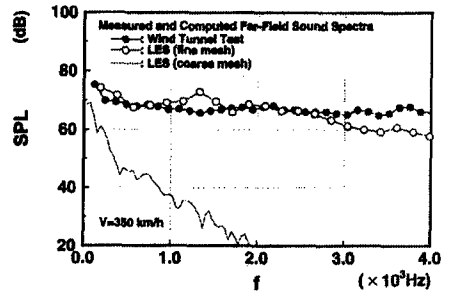
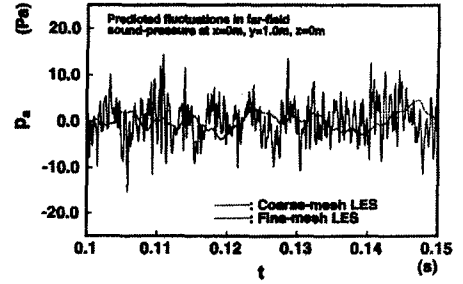


Figure 18. Computed far-field sound-pressure fluctuations (upper) and their power spectra (lower).

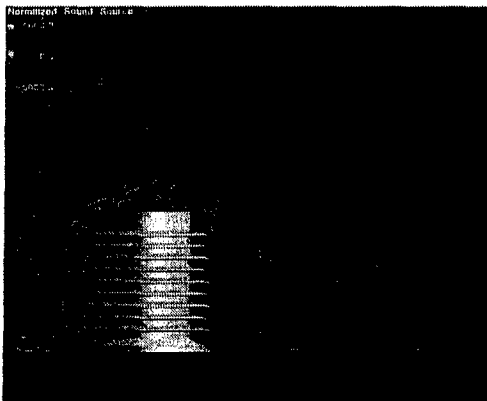


Figure 19. Instantaneous sound-source distributions in the near wake: center-line plane (left), and a plane one diameter downstream from the insulator (right).